

INVESTIGATION OF THE HIGH-ENERGY EMISSION FROM THE MAGNETAR-LIKE PULSAR PSR J1119-6127 AFTER THE OUTBURST

LUPIN CHUN-CHE LIN¹, HUI-HUI WANG², KWAN-LOK LI³, JUMPEI TAKATA², CHIN-PING HU⁴, C. Y. HUI⁵, A. K. H. KONG⁶, PAK-HIN T. TAM⁷, C.-Y. NG⁴, AND PAUL K. H. YEUNG⁸

¹ Department of Physics, UNIST, Ulsan 44919, Korea; lupin@unist.ac.kr

² School of physics, Huazhong University of Science and Technology, Wuhan 430074, China.

³ Department of Physics and Astronomy, Michigan State University, East Lansing, MI 48824, USA

⁴ Department of physics, The University of Hong Kong, Pokfulam Road, Hong Kong

⁵ Department of Astronomy and Space Science, Chungnam National University, Daejeon 305-764, Korea

⁶ Institute of Astronomy, National Tsing Hua University, Hsinchu, Taiwan

⁷ School of Physics and Astronomy, Sun Yat-sen University, Zhuhai 519082, China and

⁸ Institute of Experimental Physics, Department of Physics, University of Hamburg, Luruper Chaussee 149, D-22761 Hamburg, Germany

Draft version October 12, 2018

ABSTRACT

We performed a complete investigation on the magnetar-like radio pulsar PSR J1119–6127 with the archival high-energy observations obtained after its magnetar-like outbursts in the end July of 2016. The X-ray pulsations can be described by the contribution from two hotspots, and the surface emission from the larger hotspot can be replaced by the magnetized atmospheric radiation. After the bursts, specific regions on the neutron star can be heated up to > 1 keV, and a hard non-thermal component related to the magnetospheric emission can be seen from the spectra in the hard X-ray band. Instead of the cooling down, we find that the thermal emitting region gradually shrunk following the decrease of the source flux after the burst. Marginal hard X-ray pulsations can be detected soon after the outburst, but the signal totally disappeared in a few days. We found that the gamma-ray emission was suppressed during the outburst. This is likely caused by the reconfiguration of the magnetic field of PSR J1119–6127 accompanying with the mode changing in radio pulsation after the burst. Due to the possible global change in the magnetosphere, the timing solution of the pulsar evolved dramatically and the gamma-ray pulsation soon after the these X-ray bursts cannot be resolved without seriously counting the effect of timing noise. Unlike the exponential recovery trend of the spin-down rate that was observed in the 2004 and 2007 glitch events and the glitch events of other pulsars, we did not obtain a similar timing behavior after the glitch of 2016 caused by the bursts. We argue that temporal/spectral behaviors of the observed emission from radio to gamma-ray bands after the burst were caused by a complex combinations of a change of the magnetospheric structure, pair plasma injection and the shrinking emission sites on the neutron star.

Subject headings: methods: data analysis — pulsars: individual (PSR J1119-6127) — X-rays: bursts — radiation mechanisms: non-thermal — gamma rays: stars — magnetic fields

1. INTRODUCTION

Among the currently known pulsars, magnetars are in a special class with a relatively slow spin period and extremely strong surface magnetic field of $10^{14} - 10^{15}$ G although some of them only have relatively weak magnetic field (e.g., $\sim 6 \times 10^{12}$ G for SGR 0418+5729; Rea et al. 2013). One of the most intriguing features for a magnetar is the occurrence of bursts (Woods & Thompson 2006; Ng et al. 2011; Pons & Rea 2012) when the local magnetic stress becomes too strong to be balanced by the restoring force of the crust and the high-energy emission is powered by the decaying field (Thompson & Duncan 1996). Some rotation-powered pulsars (RPPs) with a high surface magnetic field strength ($\geq 4 \times 10^{13}$ G; hereafter, high-B pulsars) show similar outburst activities and are now treated as the transitional objects between the canonical RPPs and the magnetars (Ng & Kaspi 2011). Most high-B pulsars were discovered in the radio band (e.g., PSR J1718–3718: Hobbs et al. 2004; PSR J1814–1733: Camilo et al. 2000 and PSR J1847–0130: McLaughlin et al. 2003) and a few of them are radio-quiet (e.g., PSR J1846–0258: Archibald et al. 2008). Similar to some transient magnetars (e.g.,

1E1547.0–5408; Burgay et al. 2009), we can also detect the intermittent and variable radio pulses (Thompson 2008) on high-B pulsars. High-B pulsars and magnetars also share similar features in their outburst activities, glitch sizes and the derived timing noises. Studies on high-B pulsars may play an important role to unify the relationship between the magnetars and the isolated neutron stars/radio pulsars (Perna & Pons 2011). Among the known high-B pulsars, PSR J1119–6127 is the most attractive case because it has a confirmed rotational period of ~ 408 ms detected in the radio (Camilo et al. 2000), X-ray (Gonzalez et al. 2005) and γ -ray (Parent et al. 2011) bands for a multi-wavelength investigation.

PSR J1119–6127 is associated with the supernova remnant (SNR) G292.2–0.5 (Pivovarov et al. 2001), and its PWN was resolved by *Chandra* (Gonzalez & Safi-Harb 2003). Based on the measurements through HI absorption to the SNR, the distance of the pulsar is inferred to be 8.4 kpc away (Caswell et al. 2004). Accompanying with the detected spin down rate $\dot{P} = 4.0 \times 10^{-12}$ (Camilo et al. 2000), the inferred surface magnetic field (B) is 4.1×10^{13} G and the spin-

down luminosity is $\dot{E} = 2.3 \times 10^{36}$ ergs s^{-1} . The characteristic age can also be estimated as 1600 years with the breaking index 2.684 ± 0.002 determined by the radio timing data over 12 years (Weltevrede et al. 2011). PSR J1119–6127 experienced two glitches in 2004 and in 2007 (Weltevrede et al. 2011; Antonopoulou et al. 2015). While half of the glitches detected on magnetars coincide with energetic γ -ray flares/X-ray bursts (Dib & Kaspi 2014), no burst event was captured together with the detection of 2004 and 2007 glitches for PSR J1119–6127. Some magnetars also present a post-glitch recovery of the spin-down rate, which were also observed in the old glitches of PSR J1119–6127 (Weltevrede et al. 2011).

The Gamma-Ray Burst Monitor of the *Fermi* Observatory was triggered by a magnetar-like burst of PSR J1119–6127 on July 27th of 2016 (Younes et al. 2016), and *Swift*/Burst Alert telescope also reported a similar burst in a few hours (Kennea et al. 2016). X-ray pulsations were subsequently detected by the X-Ray Telescope (XRT) onboard the *Swift* observatory (Antonopoulou et al. 2016), and several investigations were performed for its timing and spectral behavior in the post-burst stage (Archibald et al. 2016b; Majid et al. 2016). Based on the detailed examination with S/N-based search and Bayesian blocks algorithm, 13 short X-ray bursts can be identified between July 26th and 28th of 2016 with a thermal cooling trend (Göğüş et al. 2016). The revision of the pulsar ephemeris after the outburst and a spin-up glitch of $\Delta\nu = 1.40(2) \times 10^{-5}$ Hz and $\Delta\dot{\nu} = -1.9(5) \times 10^{-12}$ Hz s^{-1} were soon determined in 2016 (Archibald et al. 2016a). The subsequent follow-up radio observations do not have any indication of the radio emission. Radio pulsation can be resolved again across a large frequency band with different profiles starting from the mid. Aug. of 2016 (Majid et al. 2017). Such a transient radio emission feature might be associated with the glitching activity as seen from magnetars (Camilo et al. 2006). In addition to the change of the pulse profiles in the different radio bands, a significant discrimination of the radio pulse profile can be detected before and after the outburst. The pre-burst radio profile presents a single pulse at 1.4 GHz while a multi-component emission structure can be detected in the profile in the same radio band after the outburst (Archibald et al. 2017). The radio pulse profiles obtained at 2.3 GHz and 8.4 GHz also displayed a different structure in mid. Aug. and early Sep. of 2016 (Majid et al. 2017), and three additional very-short X-ray bursts occurred within 70 s were identified on Aug. 30th (Archibald et al. 2017). All the observed features including the burst behavior and the unusual change of the radio profiles and variabilities exhibit high similarities to the known transient magnetars, and the detected high-energy outbursts of PSR J1119–6127 were connected to magnetar-like bursts.

Before the magnetar-like bursts, the X-ray spectrum of PSR J1119–6127 can be modelled with a thermal plus a non-thermal component (Gonzalez et al. 2005; Safi-Harb & Kumar 2008; Ng et al. 2012). The thermal emission can be attributed by a hotspot with the temperature of ~ 0.21 keV or the atmospheric emission with the temperature of 0.06–0.17 keV, and the non-thermal component of the pulsar can be described by a photon index of 1.6–2.1 with a large uncertainty. A

power-law with an exponential cutoff (PLEC) can characterize the γ -ray spectrum of PSR J1119–6127 and it behaved similar to general RPPs detected in the γ -ray band (Parent et al. 2011). The behavior of the X-ray spectrum obtained during and after the magnetar-like bursts might depend on the observing epoch. In the end July of 2016, a major thermal component and an additional power-law component of a harder photon index of 1.2 ± 0.2 is required to extend the spectrum to the hard X-ray band (Archibald et al. 2016a). The burst luminosity inferred in the X-ray band of 0.5–10 keV is 3.5×10^{35} ergs s^{-1} , corresponding to $\sim 15\%$ of the spin-down power and comparable with the luminosity in the γ -ray band of > 0.1 GeV derived in the pre-burst stage (Parent et al. 2011). In the end Oct. of 2016, a single power-law is sufficient to model the X-ray spectrum of PSR J1119–6127 with a softer photons index of 2.0 ± 0.2 (Blumer et al. 2017). Here we utilize the public data described in § 2 to completely investigate the high-energy emission from PSR J1119–6127, illustrate its observational features and discuss the possible emission scenarios.

2. HIGH-ENERGY OBSERVATIONS

In order to clarify the high-energy emission feature of PSR J1119–6127 after the outburst occurred in the end July of 2016, we analyzed the archival data obtained from *Swift*, *XMM-Newton* *NuSTAR* (Nuclear Spectroscopic Telescope ARray) and *Fermi* observatories to conduct the related temporal and spectral analysis. Details can be referred to the following subsections. In the timing analysis, all the photon arrival times were corrected to the barycentric dynamical time (TDB) with the JPL DE200 solar system ephemeris at the source position determined by *Chandra* (Safi-Harb & Kumar 2008) for all the datasets.

2.1. *Fermi* Data

We obtained the *Fermi* Large Area Telescope (LAT) data of Pass 8 (P8R2) in the energy range of 0.1–300 GeV. To avoid the serious contamination in timing analysis for our target in a source-crowded region, we only inspected the periodic signal using photons with the energy > 0.5 GeV (Parent et al. 2011). Photons in a circular region of interest within 20° and 1° from the position of 3FGL J1119.1-6127 determined in LAT 4-year point source catalog (Acero et al. 2015) are taken into account for spectral and temporal analysis respectively. To compare the spectral behavior before and after the magnetar-like burst, we considered the time of the LAT data distributed within 2013 November (\sim MJD 56,600)–2016 December (\sim MJD 57,750) and reduced it with *Fermi* Science tools v10r0p5 package. We selected events in the class for the point source or galactic diffuse analysis (i.e., event class 128), and considered photons collected in the front- and back-section of the tracker (i.e., evttype = 3). The Instrument response function to describe for the selected event type was defined as “P8R2.SOURCE_V6” throughout this study. We also excluded events with zenith angles larger than 90° to reduce contamination from Earth’s albedo γ -rays, and the data quality is constrained in the good-time-interval of the spacecraft (i.e., DATA_QUAL > 0). In the timing analysis, all the photon arrival times were corrected to TDB with the task of

TABLE 1
SPIN PERIODS OF PSR J1119-6127 DETERMINED BY THE X-RAY DATA AFTER 2016 OUTBURST IN THE END JULY.

Start obs. time	Instruments	Duration (ks)	ObsID	Photons	Epoch zero ^a (MJD)	Spin frequency ^b (Hz)	Z_1^2/H	chance prob.
2016-07-28	<i>Swift</i> /XRT	~ 35.4	00034632001	3846	57598	2.439842(1)	503/571	< 10 ⁻¹¹
2016-07-28	<i>NuSTAR</i> /FPM	~ 82.9	80102048002	32265	57598.5	2.4398409(2)	5820/6980	< 10 ⁻¹¹
2016-07-31	<i>Swift</i> /XRT	~ 17.9	00034632002	424	57600.2	2.43983(2)	28.6/47.6	5.4 × 10 ⁻⁷
2016-08-05	<i>NuSTAR</i> /FPM	~ 127.0	80102048004	40275	57606.0	2.4398219(1)	7670/9310	< 10 ⁻¹¹
2016-08-06	<i>XMM</i> /pn	~20.1	0741732601	25530	57606.6	2.4398214(8)	7070/7990	< 10 ⁻¹¹
2016-08-09	<i>Swift</i> /XRT	~57.6	00034632007	1376	57609.5	2.439814(2)	151/177	< 10 ⁻¹¹
2016-08-10	<i>Swift</i> /XRT	~5.9	00034632008	339	57610.25	2.43979(3)	64.5/79.9	< 10 ⁻¹¹
2016-08-14	<i>NuSTAR</i> /FPM	~170.8	80102048006	32473	57615.0	2.4397973(1)	5340/6320	< 10 ⁻¹¹
2016-08-15	<i>XMM</i> /pn	~27.9	0741732701	26060	57616.0	2.4397945(6)	7020/7850	< 10 ⁻¹¹
2016-08-26	<i>Swift</i> /XRT	~70.5	00034632010	627	57627.0	2.439746(3)	49.4/54.1	4.0 × 10 ⁻⁸
2016-08-30	<i>XMM</i> /pn	~32.5	0741732801	19904	57630.3	2.4397218(6)	4960/5540	< 10 ⁻¹¹
2016-08-30	<i>Swift</i> /XRT	~17.9	00034632011	542	57630.4	2.439720(8)	78.1/105	< 10 ⁻¹¹
2016-08-30	<i>NuSTAR</i> /FPM	~166.5	80102048008	20878	57631.0	2.4397154(2)	1810/1880	< 10 ⁻¹¹
2016-09-27	<i>Swift</i> /XRT	~6.4	00034632020	527	57658.05	2.43964(2)	72.7/99.9	< 10 ⁻¹¹
2016-12-12	<i>NuSTAR</i> /FPM	~183.3	80102048010	2118	57735.0	2.4391775(8)	175/203	< 10 ⁻¹¹
2016-12-13	<i>XMM</i> /pn	~47.5	0762032801	4053	57735.5	2.439177(1)	954/1020	< 10 ⁻¹¹

^a The time zero determined for the periodicity search.

^b The uncertainties quoted in parentheses of spin frequencies were assessed by eq. (6a) of Leahy (1987).

gtbary supported under *Fermi* Science tools.

2.2. Neil Gehrels Swift Data

We considered all the data of the XRT operated under the windowed timing (WT) mode during and after the magnetar-like outburst in the end July of 2016 to perform the timing analysis since only the WT mode observations can provide a precise time resolution of 1.76 ms to examine the spin periodicity of PSR J1119–6127. All the XRT observations were obtained from the HEASARC data archive and were further processed using XRTGRBLC in the HEASOFT package (v.6.22) to build the light curves and spectra. The source position is determined at (J2000) RA=11^h19^m14^s.26, dec.=−61°27′49″.3 based on the X-ray peak emission of the pulsar obtained from the *Chandra* observation (Safi-Harb & Kumar 2008; Blumer et al. 2017), and such a determination is also consistent to the pulsar coordinate resolved in the radio band so we also treat it as the timing position of PSR J1119–6127 in the entire study. We extracted the source counts from a box region of 15″ × 35″, which is the default setting of the XRTGRBLC task. Only photon energy in the range of 0.3–10 keV with grades 0–2 were included for further analysis. We corrected the photon arrival times to TDB for the check of the spin periodicity by the task of *barycorr* designed under HEASOFT.

2.3. XMM-Newton Data

After the burst, *XMM-Newton* observed PSR J1119–6127 on August 6th, 15th, 30th and December 13th of 2016. Each dataset has ~21.6 ks, 29.5 ks, 34 ks and 49 ks in exposures respectively. All the EPIC cameras were operated in the small window mode with thin filter. We only utilized the data obtained with pn camera to perform timing analysis because it provide enough temporal resolution (i.e., ~ 5.7 ms) to inspect the spin periodicity of PSR J1119–6127. We considered the good events with “PATTERN” for MOS1/2 cameras in the range of 0–12 to include single- to quadruple-pixel events, and those for the pn camera in the range of 0–4 to include only single and double events. All the data reduction was proceeded with the latest XMM-Newton

Science Analysis Software (XMMSAS version 16.1.0). We also filtered out artifacts from the calibrated and concatenated dataset and put the most conservative events screening criteria as “FLAG==0”. Since our target may experience a short burst (e.g., Archibald et al. 2017) or the X-ray background flare, we removed all the photons collected in these time intervals to avoid any contamination in both timing and spectral analysis.

The determined position of our target is also centered at the timing position given by the *Chandra* image as described for the reduction of *Swift* observations, and photons within a circular region of a 20″ radius centered at this position were extracted to correspond an encircling energy function of ~76%. In the corresponding analyses, we only consider the events in the energy range of 0.15–12 keV. We corrected the photon arrival times to TDB using the XMMSAS task of *barycen* for the following timing analysis. In the spectral analysis, we selected the background in the nearby source free region with the same size of our target, and generated the response matrices and ancillary response files with the XMMSAS tasks *rmfgen* and *arfgen*.

2.4. NuSTAR Data

Because X-rays emitted from PSR J1119–6127 can be heated to have higher energy after the burst, we also included the data investigated by *NuSTAR* (Nuclear Spectroscopic Telescope Array), which has the effective energy range in 3–79 keV (Harrison et al. 2013). *NuSTAR* started to observe PSR J1119–6127 following the main magnetar-like outbursts on July 28th of 2016. Excluding two slew observations and some observations with exposures less than 1 ks, we have five observations investigated on July 28th, August 5th, 14th, 30th and December 12th of 2016. Each investigation of *NuSTAR* was observed with the onboard focal plane modules A and B (FPMA/B), and has the exposures of ~54.4 ks, 87.2 ks, 95.4 ks, 92.1 ks and 94.3 ks respectively. We executed the detailed temporal and spectral analysis on the later four datasets, which are jointly observed with *XMM-Newton*. We only performed the temporal analysis of the first dataset (seq. id 80102048002) since the joint

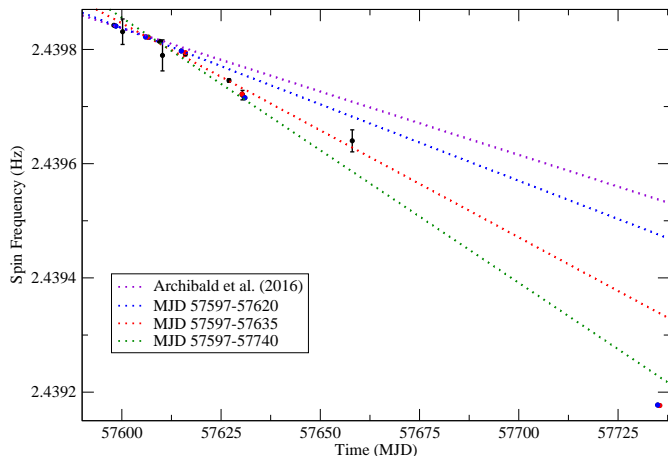


FIG. 1.— Evolution of the spin for PSR J1119-6127 determined by the X-ray archive after the 2016 magnetar-like outburst in the end July. The black, red and blue dots represent periodic signals obtained from *Swift*/XRT, *XMM*/pn and *NuSTAR*/FPM respectively. The colorful dotted lines denote the linear regression of those detections in a specific time interval as mentioned in the square frame. The violet dotted lines describe the post-outburst ephemeris determined in Archibald et al. (2016a) with spin frequency (ν) = $2.43983734(8) \text{ s}^{-1}$ and the spin-down rate ($\dot{\nu}$) = $-2.57(5) \times 10^{-11} \text{ s}^{-2}$ at the epoch of MJD 57,600. At the same epoch zero, the blue dotted line describe the best linear fit with $\nu = 2.4398376(3) \text{ s}^{-1}$ and $\dot{\nu} = -3.10(3) \times 10^{-11} \text{ s}^{-2}$ among MJD 57,597–57,620, the red dotted line show the linear fit with $\nu = 2.439846(4) \text{ s}^{-1}$ and $\dot{\nu} = -4.3(3) \times 10^{-11} \text{ s}^{-2}$ among MJD 57,597–57,635, and the green dotted line denote the linear fit with $\nu = 2.439856(4) \text{ s}^{-1}$ and $\dot{\nu} = -5.4(2) \times 10^{-11} \text{ s}^{-2}$ among MJD 57,597–57,740.

spectral fit with the *Swift* observation has been reported (Archibald et al. 2016a).

We also used the HEASOFT package (v.6.22) together with NuSTARDAS v1.8.0 and the updated *NuSTAR* calibration database (CALDB version 20171204) to proceed the related data reduction and analysis. We adopted a circular region with the radius of $60''$ (and $30''$ for the last observation, during which the source was faint) and a source-free circular region with the radius of $90''$ as the source and background extraction regions, respectively. We extracted spectra and light curves from the FPMA/FPMB observations within the pulse-invariant channel of 35–1909 corresponding to the the default energy range of 3–78 keV, and generated the corresponding response matrices by the *nuproducts* tasks. Similar to the *Swift* data, we also used the *barycorr* task to perform the barycentric time correction for following timing analysis.

3. RESULTS

We analyzed the X-ray and γ -ray data of PSR J1119-6127 mentioned in §2, and inspected the spin periodicity and spectral behavior of our target at different epochs. In the following subsections, we will present the detailed procedures in our analyses and the complete results.

3.1. Timing analysis

Based on the post-outburst ephemeris determined in Archibald et al. (2016a), we extrapolated the solution to examine the periodic signal among all the X-ray data in the nearby 100 trials using the resolution of Fourier width (i.e., $1/\text{time span}$ of the data). Only the chance probability more significant than 5.7×10^{-7} (i.e., 5σ confidence level) yielded from *H*-statistics (de Jager & Büsching

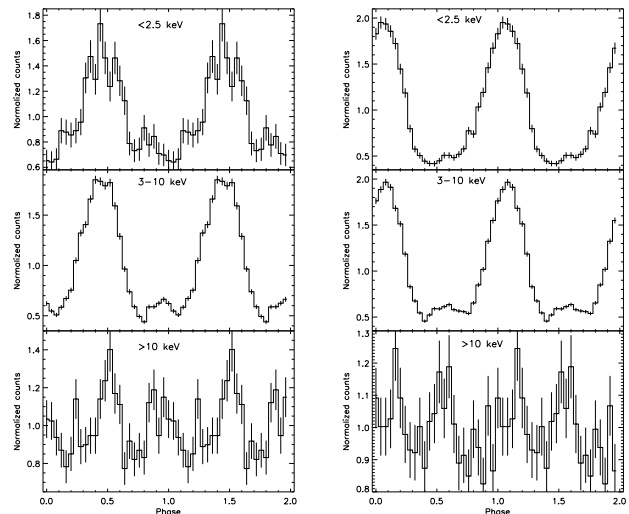


FIG. 2.— Energy-resolved pulse profiles obtained at different epochs. (a). The left panel shows energy-resolved pulse profiles generated by the *Swift*/XRT ($< 2.5 \text{ keV}$) and *NuSTAR*/FPM ($3\text{--}10 \text{ keV}$ & $> 10 \text{ keV}$) observed on July 28/29 of 2016 with the spin frequency of 2.4398409 Hz at MJD 57598.5. (b). The right panel demonstrates the energy-resolved pulse profiles generated by the *XMM*/pn ($< 2.5 \text{ keV}$) and *NuSTAR*/FPM ($3\text{--}10 \text{ keV}$ & $> 10 \text{ keV}$) observed on Aug. 5/6 with the spin frequency of 2.4398219 Hz at MJD 57606.0. Two cycles of each profile are shown for clarity.

2010) are presented in Table 1. Because the pulse profile can be mainly described by a single peak, all the results also correspond to a significant Rayleigh power (Mardia 1972; Gibson et al. 1982) except for the *Swift* data with the Obs ID. of 00034632002. The evolution of the spin frequencies detected by X-ray archive can be referred to Fig. 1, and the spin-down rate drastically increased between the end July and the mid. December of 2016.

We also checked the pulsed detection in the different energy ranges. As shown in Fig. 2, the folded light curves in the soft X-ray ($< 2.5 \text{ keV}$) and the medium X-ray ($3\text{--}10 \text{ keV}$) bands have no significant structure change with aligned pulsed peaks, and this result is consistent to that obtained in Archibald et al. (2016a). In the hard X-ray bands ($> 10 \text{ keV}$), a marginal pulsed detection with a double-peaked like shape can be determined by the data observed on 28/29 of July with a false alert prob. of 8.7×10^{-7} through *H*-statistics. Nevertheless, the hard X-ray pulsation determined by the data investigated in Aug. or after it is less than 3σ confidence level even

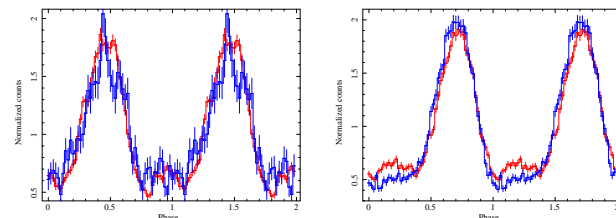


FIG. 3.— Comparison of the pulse profile obtained from the different instruments. (a). The left panel shows pulse profiles generated by the *Swift*/XRT (labelled by the blue curve) and *NuSTAR*/FPM (labelled by the red curve) with the spin frequency of 2.4398409 Hz at MJD 57598.5. (b). The right panel demonstrates the pulse profiles generated by the *XMM*/pn (labelled by the blue curve) and *NuSTAR*/FPM (labelled by the red curve) with the spin frequency of 2.4398214 Hz at MJD 57606.6. Two cycles of each profile are shown for clarity.

TABLE 2
LOCAL EPHEMERIS OF PSR J1119–6127 DERIVED THROUGH TOA
ANALYSIS THROUGH X-RAY DATA IN TABLE 1.

Parameter	
Pulsar name	PSR J1119–6127
Valid MJD range	57598–57616
Right ascension, α	11:19:14.26
Declination, δ	-61:27:49.3
Pulse frequency, ν (s^{-1})	2.4398374(1)
First derivative of pulse frequency, $\dot{\nu}$ (s^{-2})	$-2.58(4) \times 10^{-11}$
Second derivative of pulse frequency, $\ddot{\nu}$ (s^{-3})	$-9(10) \times 10^{-19}$
Third derivative of pulse frequency, $\dddot{\nu}$ (s^{-4})	$-1.3(1) \times 10^{-23}$
Epoch of frequency determination (MJD)	57600
Time system	TDB
RMS timing residual (ms)	3.5
χ^2_{ν}/dof	1.30/34
Valid MJD range	57598–57632
Pulse frequency, ν (s^{-1})	2.4398376(2)
First derivative of pulse frequency, $\dot{\nu}$ (s^{-2})	$-2.5(2) \times 10^{-11}$
Second derivative of pulse frequency, $\ddot{\nu}$ (s^{-3})	$-1.5(8) \times 10^{-18}$
Third derivative of pulse frequency, $\ddot{\nu}$ (s^{-4})	$9(3) \times 10^{-23}$
Fourth derivative of pulse frequency, $\nu^{(4)}$ (s^{-5})	$-3.9(8) \times 10^{-28}$
Fifth derivative of pulse frequency, $\nu^{(5)}$ (s^{-6})	$8(1) \times 10^{-34}$
Sixth derivative of pulse frequency, $\nu^{(6)}$ (s^{-7})	$-7.4(8) \times 10^{-40}$
RMS timing residual (ms)	3.5
χ^2_{ν}/dof	1.41/45

Note: the numbers in parentheses denote errors in the last digit

we can accumulate more hard X-ray photons with longer exposures.

To count for the influence of the timing noise, we traced the evolution of the TOA (pulse Times-of-Arrival; Ray et al. 2011) inferred from the positive detections mentioned in Table 1 with the maximum likelihood method (Livingstone et al. 2009). Because the X-ray instruments cover different effective energy range, we examine the pulse profiles generated by the same ephemeris through those data investigated with the overlapped time range to test if there is any phase difference between instruments. Fig. 3 displays examples of the comparison for the profiles generated by *NuSTAR*/FPM (in 3–78 keV) and *Swift*/XRT (in 0.3–10 keV) or *XMM*/pn (in 0.15–12 keV). There is no obvious phase lag of the major peak determined in soft X-rays or hard X-rays, so we can include all the X-ray data in TOA analysis. Each TOA was determined with enough counts (i.e., > 300) to resolve the position of the major peak in the pulse profile. To avoid the unbalanced weighting caused by lots of TOAs determined by *XMM* and *NuSTAR* in a specific/short time interval, we determined one TOA with the duration of ~ 5 -8 ks for *XMM* data and ~ 18 -20 ks for *Swift* & *NuSTAR* observations.

Among \sim MJD 57,598–57,616, two other high-order polynomial terms to describe the timing noise in the ephemeris of the pulsar are required as shown in Table 2 although the derived spin frequency and the spin-down rate is consistent to those determined in Archibald et al. (2016a). If we extend the effective time range of the pulsar ephemeris for more than half of a month, the modified solution can be referred to the bottom division of Table 2 and the timing residuals are displayed in Fig. 4. We can find that much more high-order terms to describe the timing noise are needed, and such a feature can also be applied to characterize the change of the spin-down rate

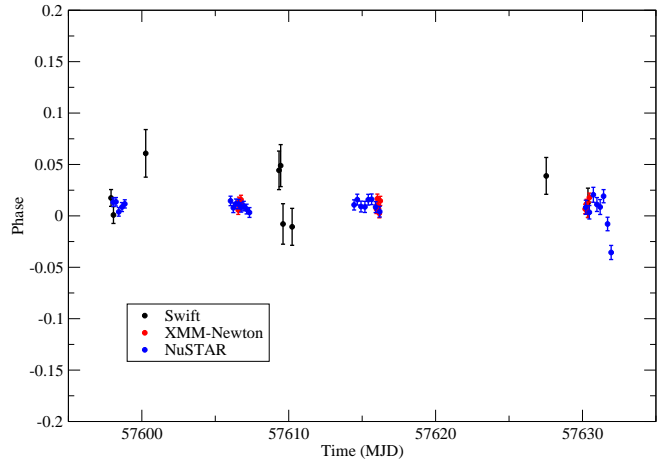


FIG. 4.— Residuals for the post-outburst timing solution of MJD 57,598–57,632. Black points are determined by *Swift*/XRT, red points are determined by *XMM-Newton*/pn and blue points label the timing residuals inferred by *NuSTAR*/FPM.

in different time interval as shown in Fig. 1. Since the next positive detection after \sim MJD 57,630 is one month later and uncertainties constrained in the timing solution is not small enough, these will lead the cycle count ambiguity for the following TOA analysis and we cannot extend the ephemeris of PSR J1119–6127 any more.

3.2. γ -ray light curve & spectrum

We performed the unbinned likelihood analysis using the “NewMinunit” optimization algorithm to derive the flux contribution of our target. Spectral parameters of other sources in region of interests (ROI) is based on the LAT 4-year point source (3FGL; Acero et al. 2015) catalog, and the standard templates of Galactic and isotropic background (gll_iem.v06.fits & iso_PSR2_SOURCE_V6.txt) were also included in our analysis. Each source including PSR J1119-6127 in ROI are freed to gain the best fit to the data, and we assumed the PLEC model to fit for the spectral behavior of our target. We divided the data into the bin of 60-day to investigate the variation of the source flux as shown in Fig. 5. Among MJD 57,570–57,630, the pulsar experienced a magnetar-like outburst, and its significance is under the resolved level so we only quote the flux upper limit in the figure. Even we consider a smaller time bin around the outburst or include lower energy band to investigate the γ -ray flux of PSR J1119-6127, we still can find that the source flux is significantly lower than its average in a long-term contribution.

The γ -ray spectrum above 0.5 GeV among MJD 57,560–57,630 for PSR J1119-6127 can be described by PLEC model with a photon index of 1.5 and a cutoff energy at 3.1 GeV. The test-statistic (TS) value (Mattox et al. 1996) is only 8.4, corresponding to a confidence level less than 3σ , and it is much less significant than the detection in other time bin. If we consider a longer accumulation time (i.e., MJD 56,900-57,560) in the pre-burst stage to derive the spectral behavior of PSR J1119-6127, the PLEC model with a photon index of 1.7 ± 0.2 and a cutoff energy at 3.1 ± 0.9 GeV can provide the best fit and it is consistent with the result obtained around the outburst at MJD 57,596. It seems that the magnetar-like outburst suppressed the γ -ray emission

from the pulsar but the major γ -ray emission mechanism did not have a significant change.

Because the post-outburst ephemeris of PSR J1119–6127 is seriously contaminated by the timing noise, it is difficult to investigate the γ -ray pulsation through the blind search. Even we built the pulsar ephemeris through the X-ray band (cf. Table 2); however, the timing solution is not long enough to accumulate enough photons to resolve the γ -ray pulsation.

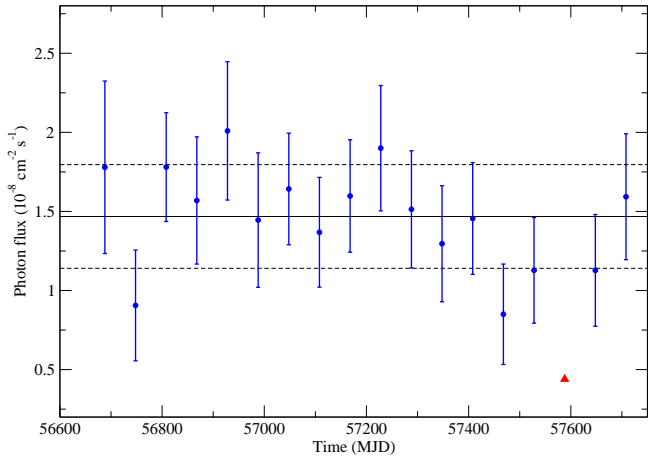


FIG. 5.— Variation of the γ -ray photon flux of PSR J1119-6127. Each data point represents the source flux above 500 MeV assessed from a 60-day accumulation of *Fermi* archive. The black solid and dashed line denotes the average flux and 1σ uncertainty of the pulsar. The source cannot be significantly resolved by the data within MJD 57,566–57,626 and we use a red triangle to label the 3σ flux upper limit.

3.3. Phase-averaged X-ray Spectral analysis

We concentrate the post-outburst spectral analysis on *XMM-Newton* and *NuSTAR* observations because *Swift*/XRT and *XMM-Newton* EPIC cover the similar energy range but the effective area of *Swift*/XRT is much smaller. The spectrum obtained from each investigation was rebinned with a minimum of different counts (e.g., 25, 50, 75 or 100) per channel to ensure the χ^2 statistics, and the choice of the minimum was decided according to the total photons received for our target.

Because the *XMM-Newton* and the *NuSTAR* data cover the similar observational time interval, we consider the joint fit with the spectra of obtained from these two observatories in the model fit. The obtained photons in the *XMM-Newton* observations with the energy less than 0.5 keV are few and the similar status can also be seen to count for photons in the *NuSTAR* observations with the energy larger than 65 keV, we therefore consider the spectral behavior of PSR J1119–6127 within 0.5–65 keV. We also introduced a constant in a simultaneous fit to account for the cross-calibration mismatch between three EPIC cameras and two different focal plane modules, and applied a photo-electric absorption using Wisconsin cross-sections (Morrison & McCammon 1983) in all the spectral fits. All the single component model cannot provide an unacceptable fit in the joint spectral fit. Except for the spectra obtained by the data of Dec. 12/13 in 2016, the composite model both of a power-law (PL) plus a blackbody radiation (BB) components

or 2BB model cannot provide an acceptable fit as well. But we notice that double BB components can provide a good fit to the spectra below 10 keV as shown in the left panel of Fig. 6, and the excess in the hard X-ray band (> 10 keV) can be described with an additional hard power-law. Even PL+BB or 2BB model can provide an acceptable fit to the spectra obtained in the mid. Dec. of 2016, such an excess in the hard X-ray band can still be clearly resolved. Fig. 6 demonstrates the fit to the spectra observed in mid. Aug. of 2016, and the right panel clearly shows that a composite model of two thermal and one power-law components (2BB+PL) can well described the observational feature.

The spectra of mid. Dec. can be described by a PL+BB model in $\chi^2_\nu = 1.05$ for 283 dof with the column absorption (N_H) of $1.9^{+0.4}_{-0.3} \times 10^{22}$ cm $^{-2}$, the photon index (Γ) of $3.4^{+0.8}_{-0.5}$ and the emission site of $0.16^{+0.02}_{-0.01}$ km in radius with a blackbody temperature of $1.18^{+0.04}_{-0.06}$ keV. All the quoted errors of spectral parameters in this article correspond to 90% confidence interval for one parameter of interest, and the distance of PSR J1119–6127 applied in the spectral model to assess the thermal emitting size is 8.4 kpc (Caswell et al. 2004). The measured photon index is softer than that described in Blumer et al. (2017) for the post-burst pulsar spectrum generated from the *Chandra* data observed in late Oct. of 2016. The unabsorbed flux derived from our spectral model in 0.5–7 keV is $(3.3 \pm 1.8) \times 10^{-12}$ ergs cm $^{-2}$ s $^{-1}$, which is about 30%–50% lower than that measured 1.5 months ago. The non-thermal component can be depicted by the magnetospheric emission of the pulsar; however, the soft X-ray photons (i.e., < 2.5 keV) of this component occupying a substantial fraction of the total source counts contribute a significant pulsed detection, and they favor a thermal origin. Because the PL+BB model cannot provide acceptable fits to the post-burst spectra obtained in the Aug. of 2016 and the physical origin in unreasonable, we rejected it in our investigations.

Table 3 lists the best parameters of the three components model in the cross-calibration fit to the joint spectra with an invariant measured absorption yielded from different detectors of *XMM-Newton* and *NuSTAR* at different epochs. Different from post-burst spectral fits to *NuSTAR* and *Swift*/XRT data described in Archibald et al. (2016a), we cannot obtained an acceptable fit with PL+BB model except for the spectra obtained in mid. December. Even we consider the PL+BB model to fit the spectra of Dec. 12/13 in 2016, the obtained photon index depicts a totally different spectral behavior in the non-thermal component. If we only consider the spectra generated by *NuSTAR* observations in 3–65 keV, the composite model with a hard PL and a single BB components can give good fits and it may mention that only the *XMM-Newton* data obtained by the larger effective area can resolve the second blackbody component in the soft X-ray band.

The double BB components determined in the composite model can be characterized by a smaller emission site (i.e. $\lesssim 1$ km in radius) with a higher temperature of ~ 1.0 keV and a larger emission site of a few kilometers in radius with a lower temperature of 0.3–0.4 keV. The absorption determined with double BB components is $1.46^{+0.06}_{-0.07} \times 10^{22}$ cm $^{-2}$, and this value is also between the

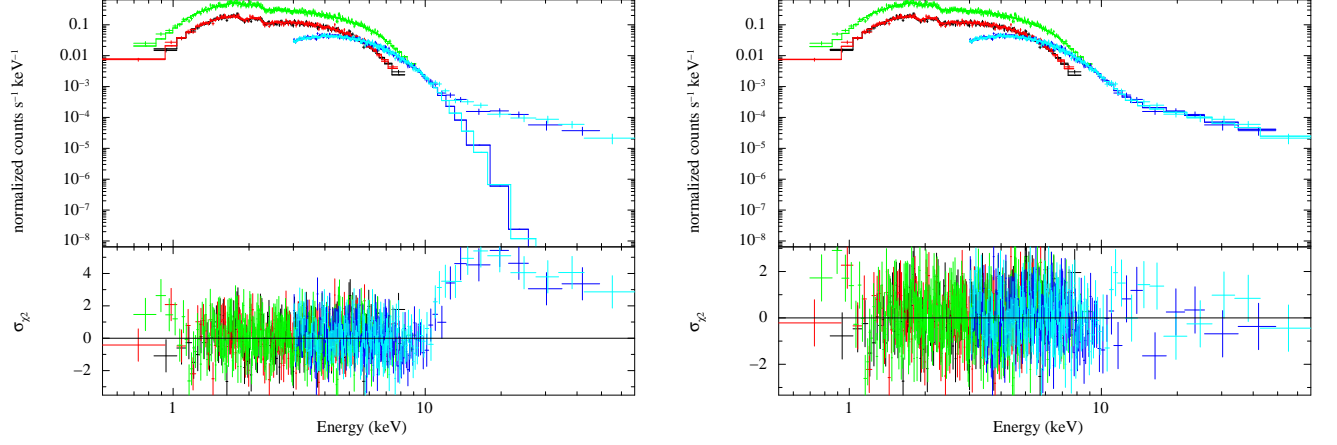


FIG. 6.— Cross-calibration fits to joint spectra with the composite model. The joint spectra include the data points obtained from *XMM-Newton*/mos1 (black color), *XMM-Newton*/mos2 (red color), *XMM-Newton*/pn (green color), *NuSTAR*/FPMA (blue color) and *NuSTAR*/FPMB (cyan color) on Aug. 14th–15th of 2016. (a). The left panel displays the fit to the composite model of double blackbody (2BB) components. (b). The right panel presents the fit to the same model with an additional power-law component (2BB+PL). Both of the bottom panels describe the residuals in terms of σ_x with error bars of size 1.

absorptions determined in Archibald et al. (2016a) and Blumer et al. (2017). If we consider the joint spectral fit without a coherent absorption, then the best fit obtained with the observation of late Aug. in 2016 gives a relatively lower absorption of $(1.3 \pm 0.1) \times 10^{22} \text{ cm}^{-2}$. We find that the determined temperatures of two hotspots can be a little lower and emission sizes can be larger if we fix a higher hydrogen absorption in the spectral fit. Except for the blackbody emission, we also considered the thermal X-rays emitted from a hydrogen atmosphere of a neutron star (nsa; Zavlin et al. 1995) and from the neutron star atmosphere with strongly magnetized hydrogen or ionized heavy element plasma (nsmax; Ho et al. 2008). Because PSR J1119–6127 has strong magnetic field of $\sim 4.1 \times 10^{13} \text{ G}$, we assumed a magnetic field strength of the same order (i.e., 10^{13} G) in both the ‘nsa’ and the ‘nsmax’ models. Comparing with the 2BB components in the composite model, only the thermal component contributed from a larger size can be replaced by the emission from the magnetized atmosphere and the determined interstellar absorption is consistent to that obtained by the fit to nsa+PL model using the pre-burst *Chandra* observations (Safi-Harb & Kumar 2008). If we considered the change of the absorbed column density at different epochs for spectral fits to the nsa+BB and the nsmax+BB model, the best fits to both models give a relatively higher value of $\sim (1.8 - 2.0) \times 10^{22} \text{ cm}^{-2}$ in mid. Dec. of 2016.

Among the spectral fits to a composite model with double BB components shown in Table 3, we did not find an obvious trend in the decrease of the temperature as presented in Archibald et al. (2016a). We can find a trend that both hotspots shrunk and decreased their contribution in flux after the magnetar-like burst. The evolution of the flux ratio between the hotter and the cooler component may indicate that the surface emission from the hotter spot gradually vanished. The decrease of the temperature can be detected if we replaced the cooler thermal component by the global atmospheric emission with a uniform temperature.

3.4. Phase-resolved X-ray Spectral analysis

TABLE 3
BEST-FIT SPECTRAL PARAMETERS FOR PSR J1119–6127
DETERMINED BY *XMM-Newton* AND *NuSTAR* DATA.

Observed Time	Aug.05/06	Aug.14/15	Aug.30/31	Dec.12/13	
$^a) N_H$		$1.46^{+0.06}_{-0.07}$			
PL	Γ	0.5 ± 0.2	$0.2^{+0.3}_{-0.2}$	0.5 ± 0.2	$-0.6^{+1.2}_{-1.4}$
+	$^b) F_{\text{PL}}$	0.023	0.010	0.020	0.001
+	kT_1 (keV)	0.33 ± 0.02	$0.34^{+0.01}_{-0.02}$	0.33 ± 0.02	$0.35^{+0.02}_{-0.03}$
BB ₁	R_1 (km)	$4.4^{+0.8}_{-0.7}$	$4.0^{+0.7}_{-0.6}$	$3.6^{+0.7}_{-0.6}$	$1.7^{+0.4}_{-0.3}$
+	$^b) F_{\text{BB}_1}$	0.34	0.28	0.21	0.058
BB ₂	kT_2 (keV)	1.03 ± 0.01	1.04 ± 0.01	1.03 ± 0.01	1.09 ± 0.04
	R_2 (km)	0.98 ± 0.02	0.81 ± 0.02	0.67 ± 0.02	0.21 ± 0.02
	$^b) F_{\text{BB}_2}$	1.60	1.16	0.75	0.091
	$\chi^2_{\nu}/\text{d.o.f.}$	$1.13/2905$			
$^a) N_H$		1.52 ± 0.03			
PL	Γ	0.5 ± 0.2	$0.2^{+0.2}_{-0.3}$	$0.5^{+0.2}_{-0.3}$	$0.2^{+1.8}_{-1.1}$
+	$^b) F_{\text{PL}}$	0.022	0.010	0.019	0.003
$^c) \text{nsa}$	kT_1 (eV)	234^{+4}_{-3}	224^{+4}_{-3}	210 ± 3	162^{+2}_{-6}
+	$^b) F_{\text{nsa}}$	0.44	0.36	0.28	0.086
BB	kT_2 (keV)	1.03 ± 0.01	1.04 ± 0.01	1.03 ± 0.01	$1.03^{+0.03}_{-0.04}$
	R (km)	$0.97^{+0.01}_{-0.02}$	$0.81^{+0.01}_{-0.02}$	$0.67^{+0.01}_{-0.02}$	$0.24^{+0.01}_{-0.02}$
	$^b) F_{\text{BB}}$	1.59	1.16	0.74	0.096
	$\chi^2_{\nu}/\text{d.o.f.}$	$1.14/2909$			
$^a) N_H$		$1.55^{+0.04}_{-0.02}$			
PL	Γ	$0.5^{+0.2}_{-0.3}$	$0.1^{+0.3}_{-0.2}$	$0.4^{+0.3}_{-0.2}$	$0.2^{+2.8}_{-1.2}$
+	$^b) F_{\text{PL}}$	0.021	0.0095	0.018	0.0030
$^d) \text{nsmax}$	kT_1 (eV)	250 ± 4	240^{+3}_{-4}	224^{+4}_{-3}	172^{+3}_{-13}
+	$^b) F_{\text{nsmax}}$	0.49	0.41	0.31	0.095
BB	kT_2 (keV)	1.03 ± 0.01	1.05 ± 0.01	1.03 ± 0.01	$1.04^{+0.03}_{-0.05}$
	R_2 (km)	$0.96^{+0.01}_{-0.02}$	$0.80^{+0.01}_{-0.02}$	$0.66^{+0.01}_{-0.02}$	$0.23^{+0.02}_{-0.01}$
	$^b) F_{\text{BB}_2}$	1.57	1.15	0.74	0.095
	$\chi^2_{\nu}/\text{d.o.f.}$	$1.14/2909$			

$^a)$ The linked absorbed column density is in units of 10^{22} cm^{-2} .

$^b)$ The unabsorbed flux is measured in 0.5–10 keV and recorded in units of $10^{-11} \text{ ergs cm}^{-2} \text{ s}^{-1}$.

$^c)$ The mass of $1.4 M_{\odot}$, the magnetic field of 10^{13} G , and the emitting size of 13 km in radius to count for light bending (Beloborodov 2002) are considered in this model.

$^d)$ $1.4 M_{\odot}$ in mass and 10 km of radius in size is used to derive the gravitational redshift. The model parameter is fixed as 1300 for magnetar-like pulsars. The emitting size of the BB component was also assumed with 13 km in radius.

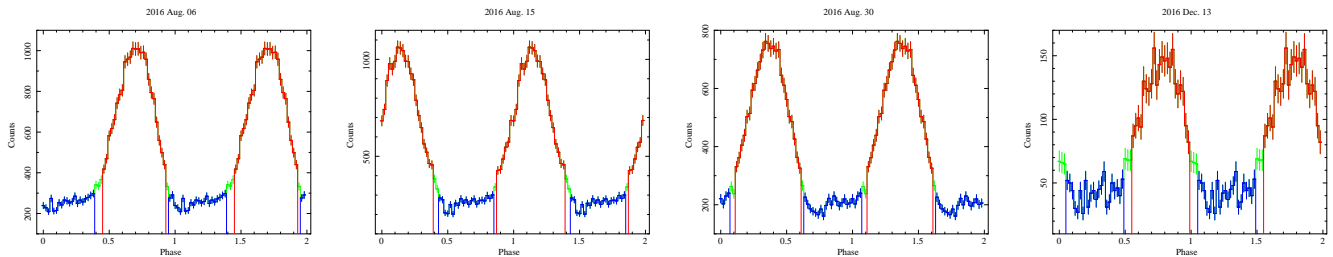


FIG. 7.— Folded light curve of PSR J1119–6127 in 0.15–12 keV obtained from four *XMM-Newton*/pn observations. Each pulse profile was generated with the spin frequency of 2.4398214 Hz, 2.4397945 Hz, 2.4397218 Hz and 2.4391766 Hz at MJD 57606.6, MJD 57616.0, MJD 57630.3 and MJD 57735.5, respectively. The region marked with the red and the blue curves represent the on-pulse and off-pulse phases in each profile. Two cycles of each profile are shown for clarity.

Based on the result of the phase-averaged spectral analysis shown in Table 3, we find that two thermal components dominate the spectral behavior in the energy range of around and less than 10 keV. The background subtracted pulsed fraction, which is determined by $(f_{max} - f_{min})/(f_{max} + f_{min}) \times 100\%$ with f_{max} and f_{min} being the maximum and minimum counts in folded bins, inferred from four *XMM-Newton*/pn data is $66 \pm 2\%$, $70 \pm 2\%$, $67 \pm 3\%$ and $87 \pm 5\%$ while it determined by *NuSTAR* observations coupling at the similar time is $65 \pm 2\%$, $61 \pm 2\%$, $49 \pm 3\%$ and $74 \pm 11\%$. Because the pulsed fraction obtained from the *XMM-Newton*/pn observation is higher and no indication of the pulsation can be detected > 10 keV after the end July, we speculate that the connection of the additional PL component required in the joint spectral analysis with *NuSTAR* observations has weak connection to the pulsation of the PSR J1119–6127. Furthermore, no significant hard X-ray pulsation can be detected after the end July of 2016. Accordingly, we only consider to generate the pulsed spectra of different epochs from the *XMM-Newton*/pn observations.

As shown in Fig. 7, we defined the phase intervals of 0.46-0.92, 0.88-1.38, 0.12-0.60 and 0.56-0.98 in related pulse profiles as the “on-pulse” components for data observed on Aug. 6th, Aug. 15th, Aug. 30th and Dec. 13th of 2016, respectively. The “off-pulse” (i.e., DC level) interval in the folded light curve was then determined at the phase within 0.96-1.38, 0.44-0.84, 0.64-1.06 and 0.06-0.48 for data observed on Aug. 6th, Aug. 15th, Aug. 30th and Dec. 13th of 2016, respectively. We generated pulsed spectra at different epochs by subtracting the spectrum of the “off-pulse” phase from that of the “on-pulse” phase. In order to ensure the χ^2 statistics, we re-grouped channels of each pulsed spectrum to have at least 50, 80, 50 and 25 photons per channel for each observation gained from early Aug. to mid. Dec. of 2016. We also generated the unpulsed spectra by subtracting the background contribution from the source spectrum gained within the “off-pulse” interval as defined in Fig. 7 while the background spectrum was determined by the nearby source free region. The unpulsed spectrum is also rebinned with a minimum of 25, 40, 25 and 15 counts per channel for each data observed from early Aug. to mid. Dec. of 2016.

3.4.1. Pulsed Spectral Analysis

Most of investigations to fit for the individual pulsed spectrum with a single PL or a single BB component obtain an unacceptable or a poor result. Although the

TABLE 4
BEST-FIT PARAMETERS FOR THE PULSED SPECTROSCOPY OF PSR J1119–6127 DETERMINED BY *XMM-Newton*/PN DATA.

Observed Time	Aug. 06	Aug. 15	Aug. 30	Dec. 13
$a) N_H$	0.85 ± 0.04			
BB kT (keV)	1.01 ± 0.02	0.96 ± 0.02	$0.93^{+0.02}_{-0.03}$	0.79 ± 0.05
R (km)	1.01 ± 0.04	$0.90^{+0.04}_{-0.03}$	$0.78^{+0.03}_{-0.04}$	0.40 ± 0.04
$b) F_{BB}$	1.52	1.02	0.66	0.093
$\chi^2_{\nu}/d.o.f.$	$1.25/569$			
$a) N_H$	1.8 ± 0.2			
PL Γ	$3.2^{+0.7}_{-0.5}$	3.0 ± 0.5	$2.7^{+0.6}_{-0.4}$	$3.2^{+0.7}_{-0.6}$
+ $b) F_{PO}$	1.58	1.19	0.93	0.27
BB kT (keV)	1.00 ± 0.03	$0.97^{+0.03}_{-0.04}$	$0.96^{+0.07}_{-0.09}$	$1.2^{+0.2}_{-0.2}$
R (km)	$0.99^{+0.09}_{-0.08}$	$0.81^{+0.07}_{-0.08}$	$0.58^{+0.1}_{-0.09}$	$0.13^{+0.06}_{-0.07}$
$b) F_{BB}$	1.42	0.84	0.41	0.044
$\chi^2_{\nu}/d.o.f.$	$1.10/561$			
$a) N_H$	$1.3^{+0.1}_{-0.2}$			
BB ₁ kT_1 (keV)	$0.37^{+0.12}_{-0.07}$	$0.45^{+0.10}_{-0.08}$	$0.46^{+0.11}_{-0.08}$	$0.38^{+0.06}_{-0.05}$
R_1 (km)	3^{+2}_{-1}	$2.1^{+1.0}_{-0.7}$	$1.9^{+0.8}_{-0.6}$	$1.4^{+0.6}_{-0.4}$
+ $b) F_{BB_1}$	0.24	0.25	0.24	0.060
BB ₂ kT_2 (keV)	$1.01^{+0.05}_{-0.03}$	$1.03^{+0.06}_{-0.05}$	$1.08^{+0.11}_{-0.08}$	$1.2^{+0.1}_{-0.2}$
R_2 (km)	$1.00^{+0.08}_{-0.10}$	$0.76^{+0.09}_{-0.11}$	0.5 ± 0.1	0.17 ± 0.05
$b) F_{BB_2}$	1.53	0.94	0.55	0.071
$\chi^2_{\nu}/d.o.f.$	$1.07/561$			

^{a)} The linked absorbed column density is recorded in units of 10^{22} cm^{-2} .

^{b)} The unabsorbed flux is measured in 0.5–8 keV and recorded in units of $10^{-11} \text{ ergs cm}^{-2} \text{ s}^{-1}$.

composite model of PL+BB components can provide acceptable fits to the pulsed spectra obtained at different epochs after the magnetar-like outburst, we can find that the photon index is abnormally large (i.e., > 2.5) comparing with the general non-thermal X-ray spectral behavior described for PWNe (Kargaltsev & Pavlov 2008) or pulsars (Cheng & Zhang 1999). In addition, the non-thermal component both dominates the source flux and the spectra in the soft X-ray band. Since the folded light curves obtained by *XMM-Newton*/pn at different epochs all have a pulsed fraction larger than 65%, we can infer that the dominant non-thermal component should have the contribution on pulsed emission to lead such a large pulsed fraction. The thermal emission of the pulsar is usually originated from the blackbody radiation of the surface, and the non-thermal pulsations are always corresponding to the synchrotron radiation in the magnetosphere to have a pulse profile similar to what we detected in the hard X-ray band through the *NuSTAR* observa-

tions of the end July (cf. Fig. 2). Nevertheless, we obtain the similar structure without a phase change in the energy-resolved pulse profiles less than 10 keV, and it disfavors the existence of a non-thermal scenario.

In Table 4, we present the simultaneous fit to the pulsed spectrum with 2BB components and a coherent hydrogen absorption. The thermal flux derived for two hotspots and the emission size inferred from 8.4 kpc away are marginally lower than what we obtain in Table 3, but are still statistically consistent. Because the composite model contributed by two thermal components provides a better fit and a plausible result, we prefer to explain the pulsed spectral behavior with a pure thermal origin from different sites of different temperatures. We cannot conclude a significant change in the temperature of each thermal component derived from different observations, but the shrink of both emitting regions led to the lower and lower pulsed emission evolving with time.

3.4.2. Unpulsed Spectral analysis

Different from the phase-averaged spectra and the pulsed spectra of PSR J1119–6127, the unpulsed spectra extracted from those events in the “off-pulse” can have an acceptable fit to a single BB model as presented in Table 5. However, the interstellar absorption obtained from the fit must be low to yield an acceptable fit, and it is lower than all the values defined in the previous literatures (e.g., the lowest one is $(1.1 \pm 0.1) \times 10^{22} \text{ cm}^{-2}$ determined by single BB model in Blumer et al. 2017). The input of an additional BB component in the spectral fitting can allow us to get stronger absorption as presented in Table 5. In the unpulsed spectral fit to the composite model of double BB components, we find that the application of the strong absorption in the fit leads to lower temperatures of two emission sites; for instance, the temperatures of two hotspots fitted to the spectrum generated from *XMM-Newton*/pn data of Aug. 6th in 2016 are $0.43^{+0.06}_{-0.07}$ keV and $1.18^{+0.07}_{-0.06}$ keV if we set the column density as $1.6 \times 10^{22} \text{ cm}^{-2}$. Although it is incomprehensible that both pulsed and unpulsed spectra have similar origins with similar temperatures, such emitting geometry can still exist due to the light bending.

An additional non-thermal PL combined with the thermal emission from a small hotspot can also provide acceptable fits to the spectra. Such a thermal origin cannot be replaced by the emission from the global atmosphere or we cannot receive tolerable fits to the spectrum. The best-fit parameters to the PL+BB model have a relatively stronger absorption (i.e., $(1.7 \pm 0.3) \times 10^{22} \text{ cm}^{-2}$) and a steeper photon index (i.e., $\Gamma \gtrsim 3$). Such a strong absorption was also obtained in the pre-burst spectral analysis of PSR J1119–6127, and the soft non-thermal component can be originated from the magnetospheric upscattering of the thermal photons (Thompson et al. 2002). The flux derived from the thermal and non-thermal components are comparable. We speculate that the thermal emission of the unpulsed spectroscopy owning the similar temperature (~ 1.0 – 1.1 keV) to the small hotspot existed in the pulsed spectroscopy may have the same origin, and a smaller size gained from the fit denotes that only a part of emission can be seen in the off-pulse phase because of the strong gravity.

4. DISCUSSION

TABLE 5
BEST-FIT PARAMETERS FOR THE UNPULSED SPECTROSCOPY OF PSR J1119–6127 OBTAINED FROM *XMM-Newton*/PN DATA.

Observed Time	Aug. 06	Aug. 15	Aug. 30	Dec. 13
$^a) N_H$			$0.79^{+0.04}_{-0.05}$	
BB kT (keV)	$1.09^{+0.03}_{-0.02}$	1.11 ± 0.02	1.11 ± 0.03	1.1 ± 0.1
R (km)	$0.61^{+0.02}_{-0.03}$	0.51 ± 0.02	0.41 ± 0.02	0.12 ± 0.02
$^b) F_{\text{BB}}$	0.74	0.55	0.36	0.033
$\chi^2_{\nu}/\text{d.o.f.}$			1.09/488	
$^a) N_H$			1.7 ± 0.3	
PL Γ	2.2 ± 0.5	$3.0^{+0.8}_{-0.7}$	2.9 ± 0.8	3^{+5}_{-2}
+ $^b) F_{\text{PO}}$	0.66	0.46	0.28	0.035
BB kT (keV)	$1.05^{+0.09}_{-0.10}$	$1.13^{+0.04}_{-0.03}$	$1.12^{+0.04}_{-0.05}$	1.2 ± 0.5
R (km)	$0.53^{+0.10}_{-0.08}$	0.46 ± 0.05	0.38 ± 0.04	$0.09^{+0.06}_{-0.07}$
$^b) F_{\text{BB}}$	0.48	0.49	0.31	0.023
$\chi^2_{\nu}/\text{d.o.f.}$			1.01/480	
$^c) N_H$			1.2 ± 0.2	
BB ₁ kT_1 (keV)	$0.6^{+0.2}_{-0.1}$	$0.37^{+0.11}_{-0.07}$	$0.40^{+0.15}_{-0.09}$	$0.4^{+0.6}_{-0.2}$
R_1 (km)	$1.2^{+0.6}_{-0.4}$	$1.8^{+1.4}_{-0.8}$	$1.2^{+0.5}_{-1.0}$	$0.5^{+2.3}_{-0.4}$
+ $^b) F_{\text{BB}_1}$	0.25	0.083	0.053	0.0082
BB ₂ kT_2 (keV)	$1.3^{+0.3}_{-0.1}$	$1.14^{+0.05}_{-0.04}$	$1.14^{+0.06}_{-0.05}$	$1.23^{+0.04}_{-0.18}$
R_2 (km)	$0.4^{+0.1}_{-0.2}$	$0.48^{+0.04}_{-0.05}$	$0.39^{+0.03}_{-0.05}$	$0.10^{+0.04}_{-0.10}$
$^b) F_{\text{BB}_2}$	0.58	0.54	0.35	0.031
$\chi^2_{\nu}/\text{d.o.f.}$			1.00/480	

$^a)$ The linked absorbed column density is recorded in units of 10^{22} cm^{-2} .

$^b)$ The unabsorbed flux is measured in 0.5–8 keV and recorded in units of $10^{-11} \text{ ergs cm}^{-2} \text{ s}^{-1}$.

We have performed a study to trace the high-energy timing and spectral behavior of PSR J1119–6127 after its outbursts. Because the positive detections of the X-ray pulsation after early Sep. of 2016 are few, we cannot extend a longer timing solution with the sparse data points by TOA analysis. The serious timing noise imposed on the timing behavior of PSR J1119–6127 can be resolved in the end Aug. of 2016 by comparing ephemerides determined within different time interval, and it also prohibits a direct γ -ray pulsed detection through the blind search. The one-month solution determined in Table 2 also cannot be used to confirm the γ -ray pulsation immediately after the burst of end July in 2016 because the accumulated photons of only one month extracted from *Fermi* observations are not enough to detect the pulsed emission. According to spin-down rate derived by the linear regression of different time ranges, we did not find an indication of its recovery. Instead of the recovery of the spin-down rate that can be observed after two previous glitches (Weltevrede et al. 2011; Antonopoulou et al. 2015) or after the glitch event of other high-B pulsar (Ng et al. 2011), we suspect that some events occurred in the end Aug. of 2016 may slow down the pulsar and continuously increase its spin-down rate. Three short magnetar-like X-ray bursts detected on Aug. 30 of 2016 may not only relate to the change of the radio pulse profiles (Archibald et al. 2017), but also to the increase of the timing noise and the spin-down rate of PSR J1119–6127. To clarify whether such short bursts lead to another glitch and determine the related parameters, we require more dense data points of confirmed pulsations after early September and the current information is not enough to identify it.

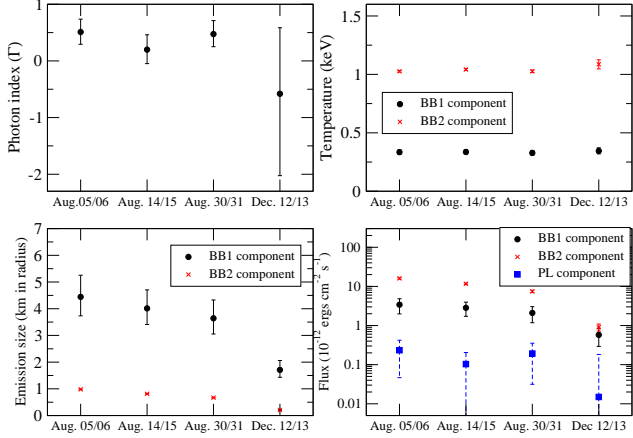


FIG. 8.— Spectral parameters obtained by the simultaneous fit to the joint spectra of *XMM-Newton* and *NuSTAR* observations with a linked absorption. The figure of each panel presents the parameters of PL+2BB model obtained from the best fit to the joint spectra of 0.5–65 keV. The value of each parameter can be referred to Table 3. The error bar denotes the 90% confidence interval.

Different from the phase-averaged spectroscopy of PSR J1119–6127 before the 2016 outbursts (Ng et al. 2012), we require two thermal components of different sizes to describe the X-rays around or less than 10 keV emitted from the pulsar. A neutron star with a strong toroidal magnetic field can lead to the discontinuities of the tangential components of the magnetic field, where the Ohmic dissipation is strongly enhanced (Viganò & Pons 2012) to affect the thermal evolution through the Joule heating rate. The conduction of heat following the aforementioned process becomes anisotropic and a neutron star presents the inhomogeneous surface temperature distributions (Viganò et al. 2013). The pulse profile can eventually evolve into a single peak profile with a high pulsed fraction (Perna et al. 2013); however, PSR J1119–6127 is a young pulsar with the characteristic age of only 1600 years. But the typical magnetothermal model assumes that the cooler surface emission can be hidden under the case of strong interstellar absorption ($N_H \gtrsim 10^{22} \text{ cm}^{-2}$), and the thermal component of the neutron star within the energy band of 0.5–2 keV only concentrates on a single hotspot of about 1–2 km (cf. simulations in Shabaltas & Lai 2012). The component of the cooler hotspot obtained in our X-ray spectral fit has a temperature of > 0.3 keV and contributes a significant fraction of photons less than 2.5 keV, so a more complete model to re-investigate how the multiple thermal components to lead a single-peaked profile is required. The contribution of cooler but larger thermal component can also be described by the global magnetized atmospheric emission with a uniform temperature. Because the cooler thermal emission also has a substantial contribution in the pulsation, we speculate the emission scenario from two local hotspots might be easier to construct the observed pulsed structure. We also note that the hotter thermal emission in the composite model can be replaced by a Comptonization component (i.e., CompBB model; Nishimura et al. 1986) to gain the comparable fit to the spectra, and the blackbody temperature of the Comptonized model is consistent to that determined for the surface emission.

Although the composite model of a PL plus a BB com-

ponents can also obtain an acceptable fit to the phase-averaged spectra, we cannot discriminate the contribution of the non-thermal component dominated in the soft X-ray pulsation (i.e., < 2.5 keV) from the thermal pulsation. Comparing with the flux of PWN detected in the post-burst stage (Blumer et al. 2017) and the required time to power it by the 2016 bursts, the flux contribution larger than $10^{-12} \text{ ergs cm}^{-2} \text{ s}^{-1}$ with a steep photon index of $\Gamma \gtrsim 3$ determined by the non-thermal component should result from the different origin even we cannot exclude the negligible contribution from PWN. Though the similar combined components can also be resolved in the pulsed spectra extracted from the *XMM-Newton* observations as shown in Table 4, a non-thermal origin to emit a large amount of soft X-ray photons without any reasonable interpretation is not preferred to describe the pulsed emission. But an additional PL component with $\Gamma < 1$ is indeed required to describe the spectral behavior in the hard X-ray band (i.e., > 10 keV) when we further include the spectra obtained by *NuSTAR* observations. Because the soft photon index (2.2 ± 0.5) determined by the spectrum of PWN in the post-burst stage (Blumer et al. 2017) is much softer, we connect this non-thermal component to the magnetospheric emission of PSR J1119–6127. This component cannot be resulted from the gap emission of the pulsar after the end July of 2016 because more than 2000 source counts with the energy larger than 10 keV only corresponds to a very low significance in the confirmation of pulsation with photon counting statistics. Such a hard component can also be detected on some persistently bright magnetars (e.g., 4U 0142+61) or from the slope change on some transient magnetars (e.g., 1E 1547.0–5408) during the outbursts (Enoto et al. 2017). The similar component with an unclear origin cannot be detected on the general RPPs; even another high-B pulsar, PSR J1846-0258 shows an obvious softening of the non-thermal emission in the outburst (Ng et al. 2008).

Both of the phase-averaged spectral and the pulsed spectral analyses did not show an obvious temperature variation on two thermal components, but we can detect a trend of the shrink in the emission site as shown in

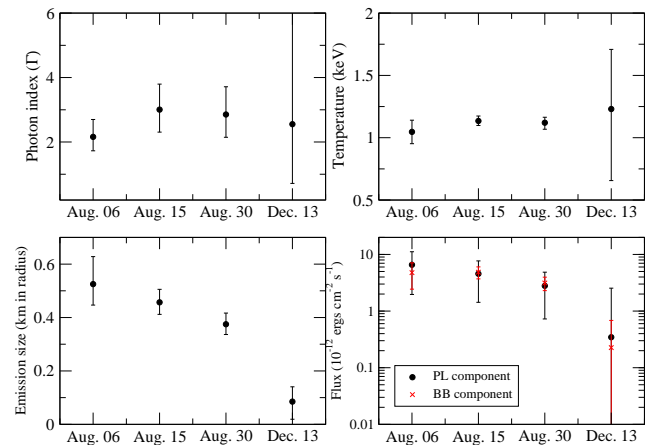


FIG. 9.— Spectral parameters obtained by the simultaneous fit to the unpulsed spectra with a PL plus a BB components with a linked absorption. The figure of each panel presents the parameters of PL+BB model obtained from the best fit to the unpulsed spectra in 0.5–10 keV. The value of each parameter can be referred to Table 5. The error bar denotes the 90% confidence interval.

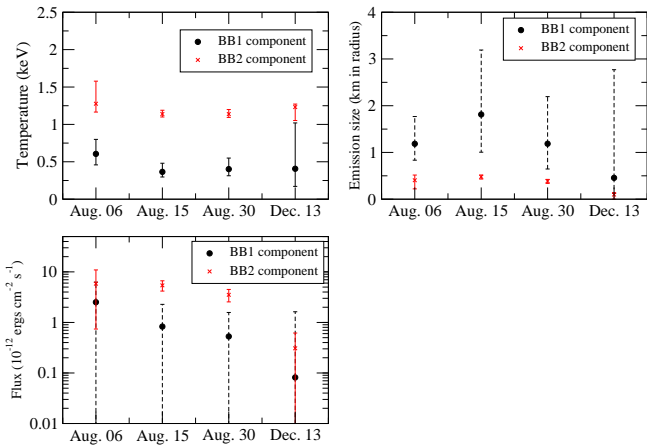


FIG. 10.— Spectral parameters obtained by the simultaneous fit to the unpulsed spectra with 2BB components with a linked absorption. The figure of each panel presents the parameters of 2BB model obtained from the best fit to joint spectra in 0.5–10 keV. The value of each parameter can be referred to Table 5. The error bar denotes the 90% confidence interval.

Fig 8. The similar feature can also be observed in the outburst decay of some magnetars (Esposito et al. 2013; Rodriguez Castillo et al. 2016). The decrease of the temperature can only be seen when the emission from the larger hotspot with the cooler temperature is substituted for that from the global atmosphere. If we apply the simultaneous fit to the pulsed spectrum with a linked absorption ($N_{\text{H}} = 1.59_{-0.09}^{+0.07} \times 10^{22} \text{ cm}^{-2}$) by the nsa+BB model, we can find the uniform temperature over the entire surface of a $1.4 M_{\odot}$ with 13 km radius changed from $245_{-9}^{+13} \text{ eV}$, $234_{-10}^{+9} \text{ eV}$, 223_{-9}^{+8} eV to 172_{-6}^{+5} eV obtained from the *XMM-Newton* data on Aug. 06, Aug. 15, Aug. 30 and Dec. 13, respectively.

In the spectral analysis to the unpulsed spectrum, both the composite models of PL+BB and 2BB can provide acceptable fits with the spectral parameters as shown in Fig. 9 and Fig. 10. The resonant cyclotron scattering of the surface thermal emission (Thompson et al. 2002) and the gravitational bending of the emission from the warmer hot spot may provide the radiative scenario of the PO+BB model. The non-thermal contribution, which dominates the soft X-ray photons (i.e., $< 2.5 \text{ keV}$), is comparable to the surface emission in this model; nevertheless, the effect of resonant Compton scattering mainly produces the hard X-ray photons and results in a disadvantage to explain the off-pulse emission with such a soft PL component. It is also strange that both pulsed and off-pulsed emission have the similar emission scenario, but we can note the emission sizes of two hotspots determined by the unpulsed spectra are smaller than those inferred from the fit to the pulsed spectrum. This result can be interpreted by that a fraction of the surface emission can be observed due to the strong gravitational deflection of light when hotspots are not in the direction of sight. Comparing with two thermal components, the emission from the PWN and magnetospheric pulsation is low and cannot be certainly resolved from the spectra without the information in the hard X-ray band (i.e., $> 10 \text{ keV}$.)

Around the X-ray outbursts of PSR J1119–6127 occurred in the end July of 2016, we found the source flux $F_{0.5-300\text{GeV}} < 4.9 \times 10^{-12} \text{ ergs cm}^{-2} \text{ s}^{-1}$, which is clearly

smaller than $(1.2 \pm 0.1) \times 10^{-11} \text{ ergs cm}^{-2} \text{ s}^{-1}$ determined in the pre-burst stage. Although the significance of the source is significantly decrease, the similar γ -ray spectral behavior can be introduced before and at the burst stages. It mentions that the acceleration mechanism to emit γ -ray photons was suppressed without a significant change in the emission geometry. The theoretical model for the evolution of the γ -ray and the X-ray emission after the burst will be fully discussed in our subsequent paper. Similar suppression after the X-ray burst can also be detected in the radio band, and no significant radio emission from the pulsar can be detected in the end July or early Aug. of 2016 (Majid et al. 2017).

The disappearance of the radio emission can be resulted from a reconfiguration of the magnetospheric structure driven by the twist or the re-connection of a pulsar’s magnetic field lines induced by the variation of crust motions (Parfrey et al. 2012; Huang et al. 2016). The time scale required for the reconfiguration of the magnetosphere is several days, and the radio emission can be switched between the bright (B-) mode and the quiescent (Q-) mode. A synchronous change in the X-ray pulsation can sometimes be discovered in mode changing radio pulsars (Hermsen et al. 2013; Mereghetti et al. 2016). The X-ray background subtracted pulsed fractions of PSR J1119–6127 determined by *NuSTAR* observations on July 28–29 in Q-mode and on Aug. 30–31 in B-mode correspond to $63 \pm 2\%$ and $49 \pm 3\%$, which may also indicate a relatively higher ratio of non-thermal contribution when radio emission is switched on. According to the joint fit with a coherent absorption in the spectral analysis, the ratio of the unabsorbed non-thermal flux to the total source flux determined in the energy range of 3–65 keV is also lower in the Q-mode with a softer photon index ($\Gamma \sim 1.2$). Even a fraction of the non-thermal emission is contributed from the PWN, we still can suppose that the emission from the magnetosphere is more active in the B-mode if the contribution from the PWN did not have a significant change at different stages. The consequent change in the spin-down rate following the mode changing (Kramer et al. 2006) is not certainly clear since the radio observations are not dense enough to clarify the time threshold of the radio active and quiescent stages. A weak indication is that the magnitude of the frequency derivative determined in the post-outburst ephemeris of Archibald et al. (2016a) is smaller than that determined in this work including the investigations when the radio pulsar is on.

Because it is difficult to evaluate the effect on the timing solution from the short magnetar-like bursts occurred in the end Aug. of 2016 (Archibald et al. 2017), we cannot definitively conclude that the greater spin-down rate is yielded due to the reconfiguration of the global magnetosphere. Another interpretation is a large amount of electro-positron pairs created in the trapped photon-pair plasma fireball to cease the entire acceleration mechanism of a neutron star (Thompson & Duncan 1995). Such a scenario was also applied to explain the sudden radio drop over a few tens of seconds coincident with the occurrence of multiple short X-ray bursts detected in the end Aug. of 2016 (Archibald et al. 2017). The series of X-ray bursts occurred in the end July of 2016 can also enhance the energy of the trapped fire ball to create the pairs to suppress the radio and high-energy

emission. The major difference after the X-ray bursts in the end July and the end Aug. may be the cooling time scale of the pair plasma in the trapped fireball because no significant radio detection was obtained until Aug. 1st of 2016 (Majid et al. 2017) and it seems that the recovery of the radio emission required longer time.

This work made use of data supplied by the LAT data server of Fermi Science Support Center (FSSC) and by the archival data server of NASA’s High Energy Astrophysics Science Archive Research Center (HEASARC). This work is supported by the National Research Foundation of Korea (NRFK) through grant

2016R1A5A1013277. H.-H. W. and J. T. are supported by National Science Foundation of China (NSFC) grants through grants 11573010, U1631103, and 11661161010. C.-P. H. and C.-Y. N. are supported by a GRF grant of Hong Kong Government under HKU 17300215P. C. Y. H. is supported by the NRFK through grant 2016R1A5A1013277. A. K. H. K. is supported by the Ministry of Science and Technology (MoST) of Taiwan through grants 105-2112-M-007-033-MY2, 105-2119-M-007-028-MY3, and 106-2918-I-007-005. P.-H. T. T. is supported by NSFC through grants 11633007 and 11661161010.

Facilities: Fermi (LAT), Swift(XRT), XMM, NuSTAR.

REFERENCES

- Acero, F., et al. 2015, *ApJS*, 218, 23
- Antonopoulou, D., Vasilopoulos, G., & Espinoza, C. M. 2016, *The Astronomer’s Telegram*, 9282
- Antonopoulou, D., Weltevrede, P., Espinoza, C. M., Watts, A. L., Johnston, S., Shannon, R. M., & Kerr, M. 2015, *MNRAS*, 447, 3924
- Archibald, A. M., Kaspi, V. M., Livingstone, M. A., & McLaughlin, M. A. 2008, *ApJ*, 688, 550
- Archibald, R. F., Kaspi, V. M., Tendulkar, S. P., & Scholz, P. 2016a, *ApJ*, 829, L21
- Archibald, R. F., Tendulkar, S. P., Scholz, P. A., & Kaspi, V. M. 2016b, *The Astronomer’s Telegram*, 9284
- Archibald, R. F., et al. 2017, *ApJ*, 849, L20
- Beloborodov, A. M. 2002, *ApJ*, 566, L85
- Blumer, H., Safi-Harb, S., & McLaughlin, M. A. 2017, *ApJ*, 850, L18
- Burgay, M., Israel, G. L., Possenti, A., Rea, N., Esposito, P., Mereghetti, S., Tiengo, A., & Gotz, D. 2009, *The Astronomer’s Telegram*, 1913
- Camilo, F., Kaspi, V. M., Lyne, A. G., Manchester, R. N., Bell, J. F., D’Amico, N., McKay, N. P. F., & Crawford, F. 2000, *ApJ*, 541, 367
- Camilo, F., Ransom, S. M., Halpern, J. P., Reynolds, J., Helfand, D. J., Zimmermann, N., & Sarkissian, J. 2006, *Nature*, 442, 892
- Caswell, J. L., McClure-Griffiths, N. M., & Cheung, M. C. M. 2004, *MNRAS*, 352, 1405
- Cheng, K. S., & Zhang, L. 1999, *ApJ*, 515, 337
- de Jager, O. C., & Büsching, I. 2010, *A&A*, 517, L9
- Dib, R., & Kaspi, V. M. 2014, *ApJ*, 784, 37
- Enoto, T., et al. 2017, *ApJS*, 231, 8
- Esposito, P., et al. 2013, *Monthly Notices of the Royal Astronomical Society*, 429, 3123
- Gibson, A. I., Harrison, A. B., Kirkman, I. W., Lotts, A. P., Macrae, J. H., Orford, K. J., Turver, K. E., & Walmsley, M. 1982, *Nature*, 296, 833
- Gonzalez, M., & Safi-Harb, S. 2003, *ApJ*, 591, L143
- Gonzalez, M. E., Kaspi, V. M., Camilo, F., Gaensler, B. M., & Pivovarov, M. J. 2005, *ApJ*, 630, 489
- Gögüş, E., et al. 2016, *ApJ*, 829, L25
- Harrison, F. A., et al. 2013, *ApJ*, 770, 103
- Hermesen, W., et al. 2013, *Science*, 339, 436
- Ho, W. C. G., Potekhin, A. Y., & Chabrier, G. 2008, *ApJS*, 178, 102
- Hobbs, G., et al. 2004, *MNRAS*, 352, 1439
- Huang, L., Yu, C., & Tong, H. 2016, *ApJ*, 827, 80
- Kargaltsev, O., & Pavlov, G. G. 2008, in *American Institute of Physics Conference Series*, Vol. 983, 40 Years of Pulsars: Millisecond Pulsars, Magnetars and More, ed. C. Bassa, Z. Wang, A. Cumming, & V. M. Kaspi, 171–185
- Kennea, J. A., Lien, A. Y., Marshall, F. E., Palmer, D. M., Roegiers, T. G. R., & Sbarufatti, B. 2016, *GRB Coordinates Network, Circular Service*, No. 19735, #1 (2016), 19735
- Kramer, M., Lyne, A. G., O’Brien, J. T., Jordan, C. A., & Lorimer, D. R. 2006, *Science*, 312, 549
- Leahy, D. A. 1987, *A&A*, 180, 275
- Livingstone, M. A., Ransom, S. M., Camilo, F., Kaspi, V. M., Lyne, A. G., Kramer, M., & Stairs, I. H. 2009, *ApJ*, 706, 1163
- Majid, W., Dobreva, T., Kocz, J., Lazio, J., Lippuner, J., Pearlman, A. B., & Prince, T. 2016, *The Astronomer’s Telegram*, 9321
- Majid, W. A., Pearlman, A. B., Dobreva, T., Horiuchi, S., Kocz, J., Lippuner, J., & Prince, T. A. 2017, *ApJ*, 834, L2
- Mardia, K. 1972, *Statistics of Directional Data*, Probability and Mathematical Statistics a Series of Monographs and Textbooks (Academic Press)
- Mattox, J. R., et al. 1996, *ApJ*, 461, 396
- McLaughlin, M. A., et al. 2003, *ApJ*, 591, L135
- Mereghetti, S., et al. 2016, *ApJ*, 831, 21
- Morrison, R., & McCammon, D. 1983, *ApJ*, 270, 119
- Ng, C.-Y., & Kaspi, V. M. 2011, in *American Institute of Physics Conference Series*, Vol. 1379, American Institute of Physics Conference Series, ed. E. Göğüş, T. Belloni, & Ü. Ertan, 60–69
- Ng, C.-Y., Kaspi, V. M., Ho, W. C. G., Weltevrede, P., Bogdanov, S., Shannon, R., & Gonzalez, M. E. 2012, *ApJ*, 761, 65
- Ng, C.-Y., Slane, P. O., Gaensler, B. M., & Hughes, J. P. 2008, *ApJ*, 686, 508
- Ng, C.-Y., et al. 2011, *ApJ*, 729, 131
- Nishimura, J., Mitsuda, K., & Itoh, M. 1986, *PASJ*, 38, 819
- Parent, D., et al. 2011, *ApJ*, 743, 170
- Parfrey, K., Beloborodov, A. M., & Hui, L. 2012, *ApJ*, 754, L12
- Perna, R., & Pons, J. A. 2011, *ApJ*, 727, L51
- Perna, R., Viganò, D., Pons, J. A., & Rea, N. 2013, *MNRAS*, 434, 2362
- Pivovarov, M. J., Kaspi, V. M., Camilo, F., Gaensler, B. M., & Crawford, F. 2001, *ApJ*, 554, 161
- Pons, J. A., & Rea, N. 2012, *ApJ*, 750, L6
- Ray, P. S., et al. 2011, *ApJS*, 194, 17
- Rea, N., et al. 2013, *ApJ*, 770, 65
- Rodríguez Castillo, G. A., et al. 2016, *Monthly Notices of the Royal Astronomical Society*, 456, 4145
- Safi-Harb, S., & Kumar, H. S. 2008, *ApJ*, 684, 532
- Shabaltas, N., & Lai, D. 2012, *ApJ*, 748, 148
- Thompson, C. 2008, *ApJ*, 688, 499
- Thompson, C., & Duncan, R. C. 1995, *MNRAS*, 275, 255
- . 1996, *ApJ*, 473, 322
- Thompson, C., Lyutikov, M., & Kulkarni, S. R. 2002, *ApJ*, 574, 332
- Viganò, D., & Pons, J. A. 2012, *MNRAS*, 425, 2487
- Viganò, D., Rea, N., Pons, J. A., Perna, R., Aguilera, D. N., & Miralles, J. A. 2013, *MNRAS*, 434, 123
- Weltevrede, P., Johnston, S., & Espinoza, C. M. 2011, *MNRAS*, 411, 1917
- Woods, P. M., & Thompson, C. 2006, *Soft gamma repeaters and anomalous X-ray pulsars: magnetar candidates*, ed. W. H. G. Lewin & M. van der Klis, 547–586
- Younes, G., Kouveliotou, C., & Roberts, O. 2016, *GRB Coordinates Network, Circular Service*, No. 19736, #1 (2016), 19736
- Zavlin, V. E., Pavlov, G. G., Shibano, Y. A., & Ventura, J. 1995, *A&A*, 297, 441